# Manganese defective clustering: Influence on the spectroscopic features of ceria-based nanomaterials

Amaral, D.C.[1]; Rocha, L.S.R.[2]; Granone, L.I.[3]; Lage, M.M.[1]; Churio, M.S.[3]; Sanchez, M.D.[4]; Longo, E.[2]; Nascimento, H.M.S.[1]; Assis, M.[5,*]; Moura, F.[1];  Ponce, M.A.[1,6,7]

[1]Advanced Materials Interdisciplinary Laboratory (LIMAV), Federal University of Itajubá (UNIFEI), Itabira, 37500-903, Brazil.

[2]Center for Research and Development of Functional Materials (CDMF), Federal University of São Carlos (UFSCar), São Carlos, 13565-90, Brazil.

[3]Department of Chemistry and Biochemistry, FCEyN/IFIMAR, CONICET, National University of Mar del Plata, Mar del Plata, B7606FWV, Argentina.

[4]Instituto de Física del Sur (IFISUR), Departamento de Física, Universidad Nacional del Sur (UNS), CONICET, Bahía Blanca, B8000CPB, Argentina.

[5]Department of Analytical and Physical Chemistry, Jaume I University (UJI), Castelló, 12071, Spain.

[6]Physics and Engineering Research Center, National University of the Center of the Province of Buenos Aires (UNCPBA-CICPBA-CONICET), Tandil, B7000GHG, Argentina.

[7]Institute of Materials Science and Technology (INTEMA), University of Mar del Plata (UNMdP), CONICET, Mar del Plata, B7606 FWV, Argentina

**Corresponding author:** marcelostassis@gmail.com

**Abstract:** The influence of manganese modification on the spectroscopic features of manganese-doped $CeO_2$ systems synthesized by the microwave-assisted hydrothermal route and their correlation with the presence of O-defective structures was verified, focusing on their interaction with poisonous atmospheres. Raman and electron paramagnetic resonance studies confirmed the presence of defective clusters formed by dipoles/quadrupoles. The number of paramagnetic species was found to be inversely proportional to the doping concentration, resulting in an increase in the $Mn^{2+}$ signal, likely due to the reduction of $Mn^{3+}$ species after interaction with CO. X-ray photoelectron spectroscopy data showed the pure system with 33% of its cerium species in the $Ce^{3+}$ configuration, with an abrupt decrease to 19%, after the first modification with Mn, suggesting that 14% of the $Ce^{3+}$ species are donating one electron to the $Mn^{2+}$ ions, thus becoming non-paramagnetic $Ce^{4+}$ species. On the other hand, 58% of the manganese species remain in the $Mn^{2+}$ configuration with five unpaired electrons, corroborating the paramagnetic feature of the samples seen in the EPR section.

**Keywords:** Mn doping, $CeO_2$, paramagnetism, oxygen vacancies.

## 1) Introduction

The cerium electron configuration (Xe) $6s^2$ $4f^2$ $5d^0$ generates two stable valence states, $Ce^{3+}$ and $Ce^{4+}$, owing to the exchange interaction phenomenon, experimentally proven by magnetic and Mössbauer studies [1], in which the individual magnetic moments of dipoles attempt to align themselves with all other magnetic moments within the material. It is worth mentioning that because of the Hund's rule and the exchange interaction energy, the element cerium exhibits an unpaired electron in the 4f orbital, giving rise to its paramagnetic feature, which is unaffected by pressures up 50GPa, as reported by Lipp, M. J. et al. [2]. This exchange interaction takes into account conduction-electron spin polarization effects and charge fluctuation contributions, which are fundamental for systems where the localized levels approach the Fermi energy [3]. Additionally, it was shown that ceria-based magnetic susceptibilities also depend on crystal field effects [4].

Cerium dioxide ($CeO_2$), or ceria, is one of the most studied Ce-based oxides in the literature, being widely applied as a catalyst, gas sensor, optical material, biomaterial, etc. [5]. The structure of $CeO_2$ can spontaneously promote the appearance of defects such as isolated cationic O-vacancies and vacancy complexes [$CeO_7.V_o^i$] (where i can be 0, +1 or +2, represented in the Kröger–Vink notation as [$CeO_7.V_o^x$], [$CeO_7.V_o^\bullet$], and [$CeO_7.V_o^{\bullet\bullet}$], respectively) – also known as vacancy clusters. These agglomerates are intricately linked to the properties of $CeO_2$ and consequently its performance in a given application. Particularly, in addition to its charge, the [$CeO_7.V_o^\bullet$] cluster has magnetic properties and, according to the literature, is formed preferentially [6–8]. Besides, the ability to release or absorb oxygen during the redox process, known as oxygen storage capacity (OSC), allows its use as both an active catalyst in a wide variety of catalytic reactions [9–11] and an essential component for the development of gas sensors aimed at environmental air monitoring. In this context, the search and development of new materials and technologies for this field of application arise from the growing need for efficient and environmental-friendly energy sources, not to mention the strict control of the atmospheric air quality in industries and household appliances [12, 13].

One way to control and modulate defects, especially vacancy clusters, is through the substitution or doping of transition metals in the $CeO_2$ structure. This can lead to the formation of defects in the forbidden region of the band gap of $CeO_2$, causing the promotion of electrons to the 4f states of Ce, which are responsible for determining the properties of this semiconductor [14, 15]. The introduction of elements with different oxidation states or ionic radius into the $CeO_2$ sub-lattice, e.g., $Ca^{2+}$, $Mg^{2+}$ and $Gd^{3+}$, has already proved to be effective in increasing the properties of this semiconductor [16–18]. Due to its electronic properties, manganese (Mn) is a dopant that has been extensively used to change the properties of semiconductors, in particular their electronic, optical, and structural properties [19]. Mn can exhibit multivalent oxidation states when $MnO_y$-$CeO_x$ solid solutions are formed. In addition to $Mn^{2+}$, both $Mn^{3+}$ and $Mn^{4+}$ ions can also enter the $CeO_x$ structure according to several reports [20–24].

Bearing this in mind, in this work we sought to promote the creation of defective clusters in the material lattice by doping it with Mn, reinforcing the n-type behavior as a consequence of the creation of O-vacancies and vacancy complexes. For this purpose, we synthesized pure and Mn-doped $CeO_2$ systems (4, 8, and 12 wt% Mn) by the microwave-assisted hydrothermal (MAH) route followed by calcination at 500 °C. The applied characterizations by X-ray diffraction (XRD), Raman spectroscopy, field emission gun scanning electron microscopy (FE-SEM), transmission electron microscopy (TEM), electron paramagnetic resonance spectroscopy (EPR), and X-ray photoelectron spectroscopy (XPS) were used to investigate the influence of Mn modification on the presence of defective structures, which were specifically examined and correlated with the multifunctionality of this element, with a particular interest in the detection of CO atmospheres.

## 2) Experimental procedures

Pure and Mn-doped $CeO_2$ ($Ce_{1-(1/2)x}Mn_xO_2$ for x = 0, 4, 8, and 12 wt% Mn) particles were prepared using the microwave-assisted hydrothermal (MAH) route. First, Cerium nitrate hexahydrate ($Ce(NO_3)_3.6H_2O$, NEON, 99%) and Manganese nitrate tetrahydrate ($Mn(NO_3)_2.4H_2O$, CRQ, analytical grade) salts were dissolved in distilled water under stirring and heating at 60 °C. Subsequently, the nitrate solution was poured into the cerium solution followed by a pH adjustment to 10. The solution was kept under stirring for 40 min for complete homogenization, and then transferred to a Teflon® vessel and inserted into the microwave equipment (2.45 GHz, 800 W). The obtained solutions were irradiated up to 100 °C at a heating rate of 10 °C/min and kept at this temperature for 8 min. Afterwards, the solutions were cooled down to room temperature and centrifuged at 2000 rpm for 45 min three times followed by a drying process in a laboratory oven at 100 °C for 48 h. Post-synthesis calcination of the powders was carried out in atmospheric air at 500 °C for 2 h at a heating rate of 10 °C/min.

XRD analysis was performed using a D/Max-2500PC diffractometer (Rigaku, Japan) with Cu Kα radiation (λ = 1.5406 Å). Raman spectroscopy was carried out on an iHR550 spectrometer (Horiba Jobin-Yvon, Japan) with a charge-coupled device detector and an Argon-ion laser (MellesGriot, USA) operating at 633 nm and a power of 200 mW. The morphologies and textures of the samples were observed using a Supra 35VP field emission scanning electron microscope operating at 10 kV (Carl Zeiss, Germany), as well as with high-resolution transmission electron microscopy (HR-TEM) using an FEI Tecnai G2-20 (200kV). Electron paramagnetic resonance (EPR) experiments were carried out at room temperature before and after CO(g) exposure (800 ppm at a pressure of 760 mmHg for 24 h) on an ELEXSYS E500T spectrometer (Bruker, Germany) provided with an ER 4102ST rectangular resonator operating in the TE102 mode at a frequency of 9.8 GHz (X-band). The following data acquisition parameters were used for the measurements: a modulation frequency of 100.00 KHz, a

modulation amplitude of 0.10 mT, a microwave power of 3.22 mW, a central field of 344.5 mT, a sweep width of 125 mT, and a time constant of 20.48 ms. A total of 1024 data points were collected per scan, and the resulting spectra were the average of 20 scans. For quantitative analyses, the total signal intensity was determined by calculating the area below the curve corresponding to the $1^{st}$ integral of the EPR spectrum. The measured intensities were standardized according to the mass of the samples. The simulation of the EPR spectra was carried out using WinSim 2002 software (NIEHS, U.S.A.). X-ray photoelectron spectroscopy (XPS) was performed on an ESCA PHI 548 spectrometer with Mg Kα non-monochromatic radiation at 250 W and 20 mA. The resolution spectra were taken at a pass energy of 50 eV and a base pressure higher than $5 \times 10^{-10}$ Torr. An electron flood gun was used for charge compensation, and the energy scale was calibrated based on the high binding energy side peak of the ceria 3d region at 916.7 V. The signal deconvolution was made using Shirley-type background subtraction and an asymmetric sum of Gaussian–Lorentzian functions. The obtained binding energies were determined with an absolute resolution of 0.5 eV. Since Ce is the dominant element, all spectra were normalized by the maximum intensity of the peak centered at 916.7 eV after background subtraction, favoring comparisons between them.

### 3) Results and discussion

XRD analyses were performed to verify the order/disorder parameters along the range and analyze the phase and purity of the synthesized samples. **Figure 1A** shows the diffractograms obtained for pure and Mn-doped $CeO_2$ samples. All samples were identified as $CeO_2$ with fluorite-type cubic phase and space group *Fm-3m*, according to the Inorganic Crystal Structure Database (ICSD), pattern #24887. No secondary phases can be observed, evidencing the high purity of the samples obtained. A more detailed analysis of the most intense diffraction peak in the (111) direction is depicted in **Figure 1B**. As verified, the addition of $Mn^{2+}$ to the structure results in a broadening, demonstrating that doping with $Mn^{2+}$ increases the degree of long-distance disorder of the $CeO_2$ structure. In order to corroborate this result, the full width at half maximum (FWHM) of this peak was calculated, ranging from 0.45° for the pure $CeO_2$ sample to 0.65°, 0.66° and 0.74° for the samples $CeO_2$:4Mn, $CeO_2$:8Mn and $CeO_2$:12Mn, respectively. From these values, we estimated the average crystallite sizes (d) using the Debye-Scherrer method. The d values were of 19.0nm, 13.2nm, 13.0nm, and 11.6nm, from the pure to the highest doping sample.

The $CeO_2$ structure is theoretically formed by slightly distorted cubic $[CeO_8]$ clusters, with each vertex containing one O atom (**Figure 1C**). Such changes can be explained by the distorted octahedral $[MnO_6]$ clusters that may be created within the $CeO_2$ structure, which alter the periodicity of the crystalline system.
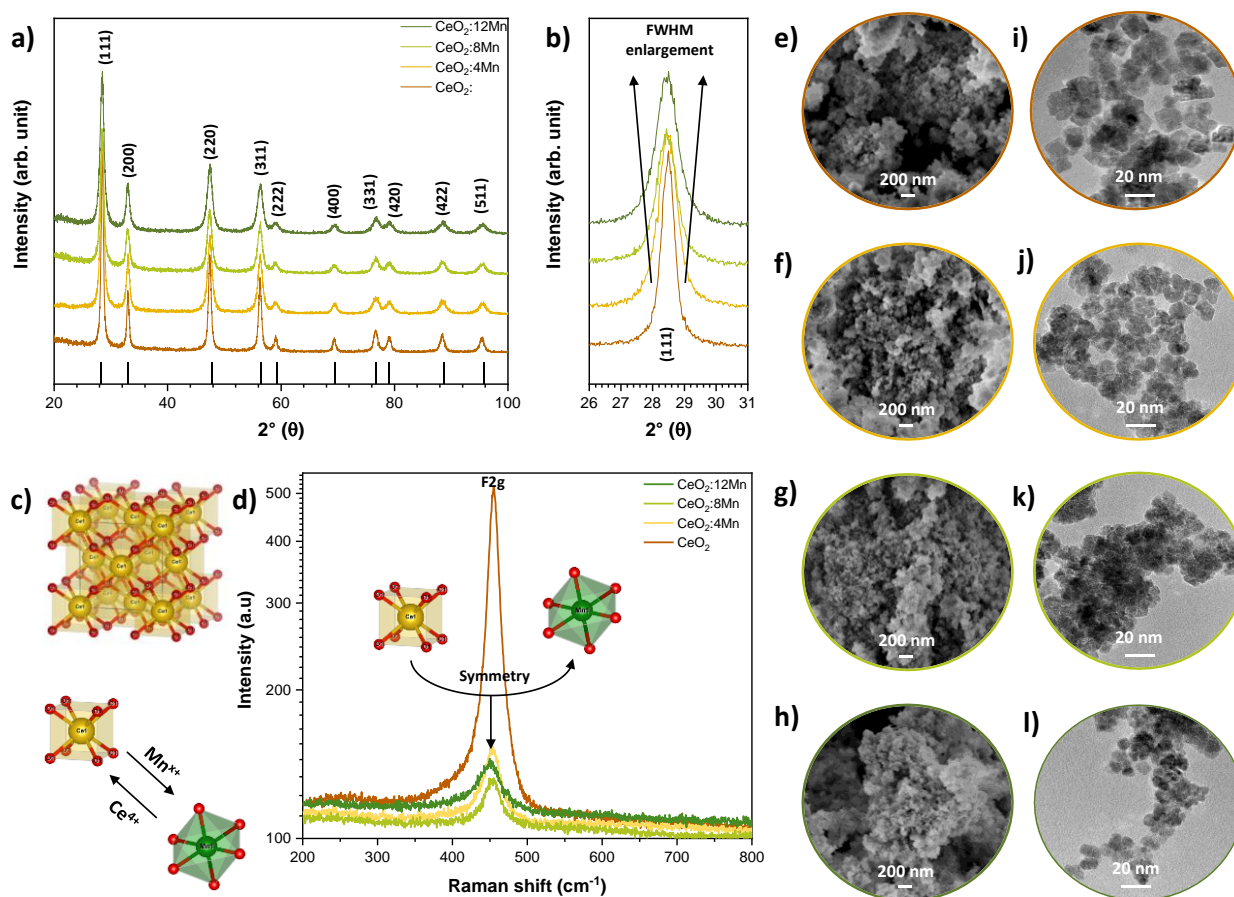
**Figure 1** – A) XRD spectra for the pure and Mn-doped samples; (B) detailed analysis of the (111) plane; (C) crystalline structure of $CeO_2$; (D) Raman spectroscopy; (E-H) FEG-SEM of the pure and doped powders after calcination at 500°C; (I-L) TEM images of the pure and doped samples.

Raman spectroscopy was used to evaluate the short-range order symmetry of the samples and corroborate the formation of defective clusters and structural defects. The results for the pure and Mn-doped samples are shown in **Figure 1D**. A clear peak around 450 cm$^{-1}$ can be observed in all samples, depicting the primary $F_{2g}$ mode, which is associated with the symmetrical stretching/breathing mode of O atoms around Ce cations [25]. As it can be seen, the pure $CeO_2$ samples have higher intensity in this mode, and the lack of any other mode indicates a highly symmetric system in both short- and long-range orders. This mode is very sensitive to any disturbance of the oxygen sublattice [26], verified by the clear reduction of its intensity when the system started to be doped [27].

This reduction can be linked to the formation of Mn [$MnO_6$] clusters, which replace the ceria [$CeO_8$] ones. These clusters have a lower electron density, owing to the presence of oxygen vacancies and their consequent non-resonant scattering of tunneling electrons [28]. Moreover, an increase in the number of electrons in the excited state is expected due to the Ce 4f$^1$, leading to variations in the

electrical properties of the semiconductor resulting from the hopping of electrons [28], in addition to their fundamental role in the interaction with adsorbed oxygen and water molecules located on the crystal surface [29, 30].

The crystallite sizes of the $CeO_2$ samples can be estimated from the Raman line broadening (FWHM) with the simple equation reported by Phokha et al. [31] and Kosacki, I. et al. [32], based on the study by Weber, Hass, and McBride [33], using a Lorentzian line-shape for the FWHM estimate. Worth mentioning that this approach can be generalized for quantitative nanoscale Raman spectroscopy [34]. According to the results, the FWHM value increases as the amount of Mn also increases in the $CeO_2$ crystalline lattice (19.2, 25.5, 25.7, and 35.5 $cm^{-1}$ for $CeO_2$, $CeO_2$:4Mn, $CeO_2$:8Mn and, $CeO_2$:12Mn, respectively). This increase can be interpreted as a significant enhancement of phonon-phonon scattering [35], which could be indicative of the creation of local distortions such as oxygen vacancies and their complexes. The crystallite sizes estimation was found to be 13.6, 8.0, 7.9, and 4.9 nm from the lowest to the highest Mn content. Worth mentioning that these values are close to the ones obtained from the XRD measurements, following the same general downtrend by increasing the Mn doping.

At this point, worth mentioning that Scherrer derived his equation for the ideal condition of a perfectly parallel, infinitely narrow, and monochromatic X-ray beam incident on a monodisperse powder of cube-shaped crystallites. Besides, It is important to note that Scherrer's equation can only be applied for average sizes up to about 100–200nm (depending on the instrument, sample, and signal-to-noise ratio) because diffraction-peak broadening decreases with increasing crystallite size and it becomes difficult to separate the peak broadening due to crystallite size from the broadening due to other factors [36]. Therefore, the slight differences between the two methods can be ascribed to the use of Lorentzian and Gaussian line shapes for the FWHM estimation as well as to the distinct proportionality constants that can be used [33].

Indeed, according to Yang and Zhang [37] the increase in the FWHM of the $F_{2g}$ mode as a function of $Mn^{2+}$ is due to the higher number of oxygen vacancies in the $CeO_2$. In this sense, Conceição et al. [38] observed a gradual increase in defects concentration by increasing the Gd content in ceria, with the charge balance being kept through the formation of oxygen vacancies with distinct charges depending on the amount of Gd.

As observed in the FE-SEM images (**Figures 1E-H**) of the pure and Mn-doped $CeO_2$ samples, there is no well-defined morphology, even after calcination at 500 ºC. The average size of the particles was calculated to be 30-40 nm, with a high degree of agglomeration, likely due to electrostatics and Van der Waals forces [39]. Indeed, from the HR-TEM observations (Figures 1I-L), the particles showed average sizes close to 20nm, which corroborates their agglomeration and the formation of clusters seen in the FEG-SEM images up to 40nm. Zhou, Y. et al. [40] were able to obtain $CeO_2$

nanoparticles (NPs) with cubic morphologies by the hydrothermal method using $Na_3PO_4.12H_2O$ as a surfactant, but at a synthesis temperature of 200 °C and a synthesis time of 20 h after calcination at 500 °C for 4 h. In this sense, the microwave-assisted hydrothermal route was found to be more advantageous for the preparation of ceria-based NPs because of the reduced costs for the synthesis procedure. Based on the analysis by Chen and Chen [41], Mn doping tends to enhance grain boundary mobility due to the large distortion of the surrounding lattice, facilitating defect migration from the matrix (i.e., $CeO_2$), an ionic radius value that is much smaller than that of $Ce^{4+}$, and the relaxation of strain induced by the substitution of $Ce^{4+}$ with ions of smaller radius [42]. Therefore, the nanometric behavior of the particles can be perceived with an overall reduction of their sizes with increasing the Mn content, which in turn inhibits grain growth due to the reduced number of effective shocks by the action of $[MnO_4]$ clusters with lower electron density. On the other hand, the replacement of $[CeO_6]$ by $[MnO_6]$ clusters increase the concentration of oxygen vacancies, inducing relaxation in the crystalline lattice.

**Figure 2** shows the EPR spectroscopy images for the samples before and after treatment with CO (Figure 2). This treatment was performed to analyze the potential of the samples to oxidize CO through a saturation of the material with CO in an atmosphere containing 760mmHg of 800 ppm of CO for 24 h at 400 °C (which is the temperature that guarantees an oxidation reaction without affecting the crystalline structure of $CeO_2$) [43]. The Mn-doped samples before CO treatment (**Figure 2A**) exhibit intense signals, which can be described as the convolution of two overlapping sextets and a broad Lorentzian curve. Both sextets, with $g$ values of 1.999 and 1.998 and average hyperfine coupling constants $A$ of 103.8 and 100.0 G, respectively, can be ascribed to the characteristic $| - 1/2, m_I> \leftrightarrow | + 1/2, m_I>$ transitions of $Mn^{2+}$ centers [44]. As it can be seen, the integrated intensity of the total spectrum increases as a function of the amount of Mn, but not linearly. Although the $Mn^{2+}$, $Mn^{3+}$, and $Mn^{4+}$ ions can enter the $CeO_2$ crystalline lattice [45], the $Mn^{3+}$ ions exhibit a large zero-field splitting, therefore being EPR-silent at conventional X-band frequencies [46, 47]. A sextet with an EPR signal similar to that of $Mn^{2+}$ but with a lower hyperfine constant $A$ (76 G) can be attributed to the presence of $Mn^{4+}$ [48]. Such signal is either absent or hidden by the intense signal of $Mn^{2+}$ ions. A broad singular line with a $g$ value of 1.94 similar to the Lorentzian curve shown in **Figure 2B** was reported as typical of $Mn^{4+}$ in $MnO_2$ samples due to dipole-dipole and exchange interactions between these ions [49]. In addition, a similar signal was described as the result of ligand field fluctuations and spin-spin interactions in highly concentrated $Mn^{2+}$ samples [50].
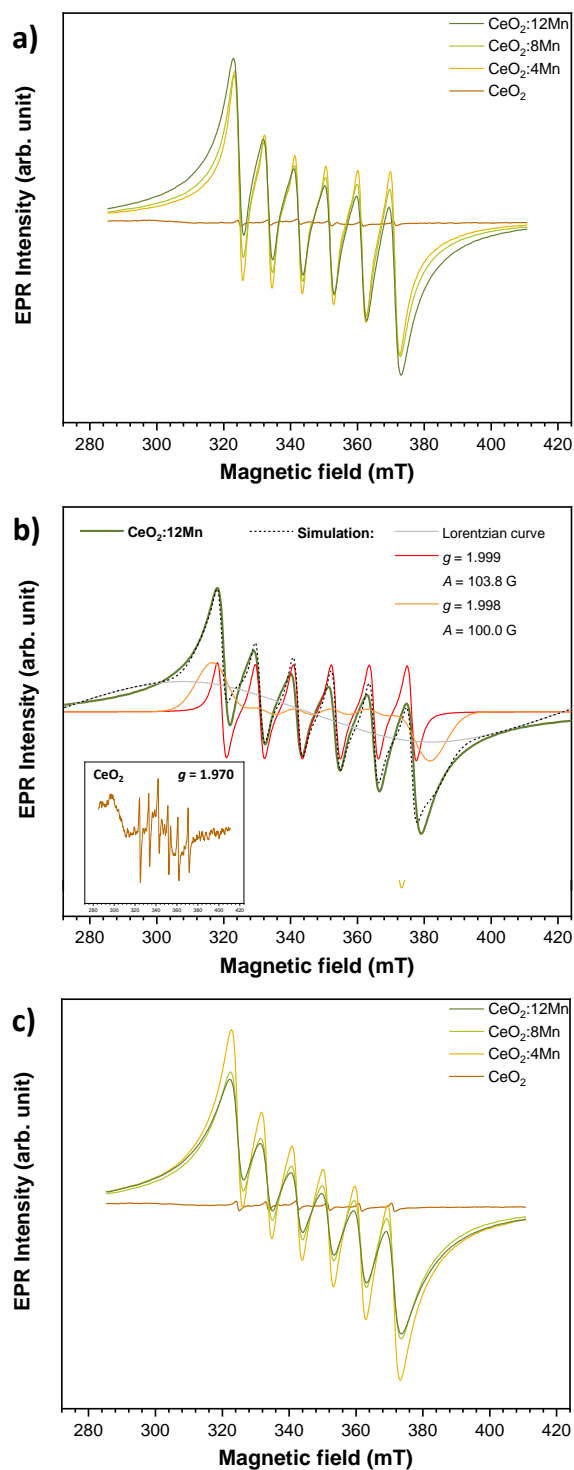
**Figure 2** – (A) EPR spectroscopy images for the samples before treatment with CO; (B) analysis of the relative contributions from the simulation procedure in comparison to the sample doped with Mn 12wt.%; (C) spectra after treatment with CO.

The analysis of the relative contributions from the simulation procedure (such as that shown in **Figure 2B**) indicates that the broad single line accounts for *ca.* 84% of the total EPR spectra for the samples not treated with CO. On this basis, $Mn^{4+}$ cannot be discarded as one of the contributing

species to the broad singlet component of the EPR spectrum, in agreement with the DFT+U calculations reported by García Pintos et al. [45]. The formation of further oxygen vacancies results in a reduction from $Mn^{4+}$ to $Mn^{3+}$ and $Mn^{3+}$ to $Mn^{2+}$. Therefore, in highly defective structures such as those reported herein, the oxidation states of Mn are mainly +3 and +2 although $Mn^{4+}$ may also be present.

After treatment with CO (**Figure 2C**), an increase in the intensity of EPR signals is observed for all samples. The increase in the $Mn^{2+}$ signal corresponds to the reduced number of oxidized species of manganese, with an oxidation state greater than +2. It can then be concluded that Mn is not only present in the +2 oxidation state, but is also in equilibrium with other higher oxidation states. Thus, manganese species must be previously oxidized during their substitution in the lattice (i.e., $Mn^{+3}$ and $Mn^{+4}$).

Valuable information concerning the oxidation state of Ce in $CeO_2$ samples can also be accessed by EPR spectroscopy. A line with a *g* value of 1.97 typically observed in $CeO_2$ samples is ascribed to electrons trapped near the surface of $Ce^{4+}/Ce^{3+}$ redox pairs [51]. Even though this signal is present in the undoped sample (inset of **Figure 2C**), as the Mn content in the samples increases, this weak line with $g \sim 1.97$ becomes negligible compared to the intense $Mn^{2+}$ signals. Therefore, it is unfeasible to analyze the evolution of the signal of trapped electrons near the surface of $Ce^{4+}/Ce^{3+}$ redox pairs with increasing the Mn concentration.

The formation of clusters of pure ceria is represented in **Figure 3A**. The scheme proposes the possibilities of interaction between the clusters that generate neutral systems as well as dipoles and quadrupoles [52–54]. As already mentioned, such oxidized configuration is a consequence of the presence of a high concentration of O-defects in the $MnO_y$-$CeO_x$ solid solutions [45]. On the other hand, $Ce^{+3}$ and $Mn^{+2}$ cations are also responsible for reducing the vacancies from $V_o^{\bullet}$ to $V_o^x$ or $V_o^{\bullet\bullet}$ to $V_o^x$, as illustrated in **Figure 3B**.
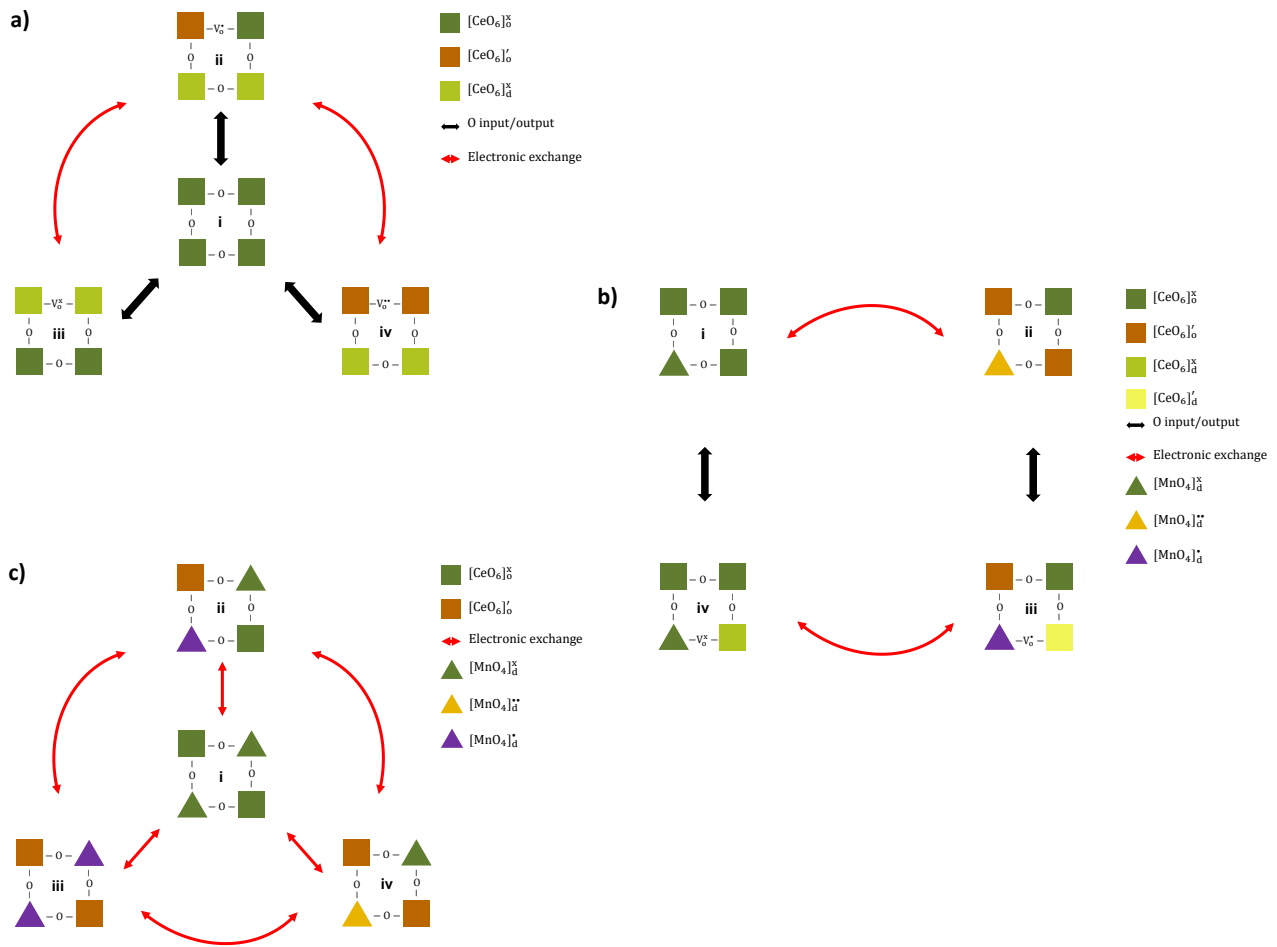
**Figure 3** – (A) Formation of clusters in the pure ceria; (B) Formation of clusters after the first introduction of $Mn^{2+}$; (C) Formation of clusters for $Mn\% > 4$ wt%.

First of all, the balance between the resonant octahedral ordered (o) and disordered (d) clusters is represented by entity (i), in which the $[CeO_6]^x$ clusters account for $Ce^{4+}$ species (**Figure 3A**). Another point that must be taken into account is the intrinsic generation of oxygen vacancies and more complex defective clusters (ii), a process that gives rise to a $[CeO_6]'$ cluster, representing $Ce^{3+}$, and a singly ionized oxygen vacancy $[V_o^\bullet]$. These $[CeO_6]'$ clusters can act as electron donors, whereas the $[CeO_6]^x$ clusters can act as electron acceptors. Singly ionized oxygen vacancies, on the other hand, can act as both electron donors and acceptors. Therefore, the electronic exchange between a singly ionized oxygen vacancy $[V_o^\bullet]$ and a $[CeO_6]^x$ cluster results in the formation of a doubly ionized oxygen vacancy $[V_o^{\bullet\bullet}]$ and an additional $[CeO_6]'$ cluster (iii), thus decreasing the $Ce^{+4}/Ce^{+3}$ ratio. In contrast, the electronic exchange between a $[CeO_6]'$ cluster and a singly ionized oxygen vacancy $[V_o^\bullet]$ generates a neutral oxygen vacancy $[V_o^x]$ and a $[CeO_6]^x$ cluster (iv), thus increasing the $Ce^{+4}/Ce^{+3}$ ratio. It is worth mentioning that the $Ce^{3+}$ species are located preferentially close to the oxygen

10

vacancies [55–57]. The mechanism presented above for the formation of neutral (iv), singly (ii) and doubly ionized (iii) oxygen vacancies was also reported in the literature by many authors [58–60].

**Figure 3B** illustrates the formation of clusters after the first introduction of $Mn^{2+}$ species $[MnO_4]^x$ into the $CeO_2$ lattice. The structure depicted in (i) can suffer from both electronic exchanges (ii) and the formation of structural defects (iv). The exchange between two electrons from an $[MnO_4]^x$ cluster and two different $[CeO_6]^x$ clusters results in the formation of an $[MnO_4]^{**}$ cluster containing $Mn^{4+}$ species and two additional $[CeO_6]'$ clusters containing $Ce^{3+}$ species (ii), while the output of an oxygen atom from the lattice generates a neutral oxygen vacancy $[V_o^x]$ (iv). Structure (iii), which contains an $[MnO_4]^*$ cluster with $Mn^{3+}$ species, can be formed either when structure (ii) forms a singly ionized oxygen vacancy or after structure (iv) undergoes an electronic exchange between a neutral oxygen vacancy and an $[MnO_4]^x$ cluster and two different $[CeO_6]^x$ clusters, thus yielding a singly ionized oxygen vacancy $[V_o^.]$, an $[MnO_4]^*$ cluster and two $[CeO_6]'$ clusters. It is noteworthy that the $[MnO_4]^x$ cluster, which has five unpaired electrons, exhibits the strongest paramagnetic behavior. Considering that part of the $Ce^{4+}$ species could reduce to the $Ce^{3+}$ configuration, this process likely stems from charges coming from $Mn^{2+}$, which in turn can generate $Mn^{3+}$ and $Mn^{4+}$ [61, 62], reducing the amount of $Mn^{2+}$ species.

When the Mn doping percentage increases, the electronic exchanges between the clusters change. **Figure 3C** shows the formation of clusters when the percentage of Mn in the lattice increases above 4 wt%. The structure, formed by $[MnO_4]^x$ and $[CeO_6]^x$ clusters containing $Mn^{2+}$ and $Ce^{4+}$ species, respectively, can undergo different electronic exchanges. The exchange between one electron from an $[MnO_4]^x$ cluster and a $[CeO_6]^x$ cluster leads to the formation of an $[MnO_4]^*$ cluster containing $Mn^{3+}$ species and a $[CeO_6]'$ cluster containing $Ce^{3+}$ (ii). The exchange between one electron from each of the two $[MnO_4]^x$ clusters and two different $[CeO_6]^x$ clusters generates two $[MnO_4]^*$ clusters containing $Mn^{3+}$ species and two $[CeO_6]'$ clusters containing $Ce^{3+}$ (iii). Finally, the exchange between two electrons from a $[MnO_4]^x$ cluster and two different $[CeO_6]^x$ clusters yields $[MnO_4]^{**}$ clusters containing $Mn^{4+}$ species and two $[CeO_6]'$ clusters containing $Ce^{3+}$ species (iv). Furthermore, structures (ii), (iii), and (iv) can be inter-converted according to the electronic exchanges depicted in **Figure 3C**. Ceria has a small magnetic moment, hence a weak paramagnetic behavior. After the formation of a ceria-based solid solution with manganese, there is a strong increase in this paramagnetic feature, which is consistent with the formation of $[MnO_4]^x$ clusters containing $Mn^{2+}$ species. However, as the amount of Mn increases, the formation of positively charged $[MnO_4]^*$ and $[MnO_4]^{**}$ clusters, which are less paramagnetic than the neutral $[MnO_4]^x$ ones, is favored. Thus, the increase in the Mn content may cause a chaotic orientation of the magnetic dipoles, deteriorating the overall paramagnetic behavior, as reported by Al-Agel et al. and Hong et al. [63, 64]. This is in agreement with our experimental results since the integrated EPR signal does not increase linearly

with the amount of Mn. Indeed, when the amount of Mn is doubled from 4 to 8 wt%, only a 20% increase in the integrated EPR signal is observed, while a further increment in the Mn content to 12 wt% results in a 35% increase.

X-ray photoelectron spectroscopy (XPS) was used to characterize the surface state and composition of the samples. **Figure S1A** displays the XPS survey spectra normalized with the Ce 3d maximum peak intensity, highlighting all observed transitions. The inset shows the XPS survey spectrum of the pure $CeO_2$ sample obtained with Mg-$K_\alpha$ radiation and the expected overlap between the Ce LMM Auger and the Mn 2p transitions. Usually, Mg-$K_\alpha$ radiation is used in $CeO_2$-based samples since the Al source leads to an overlap between the Ce Auger electrons and the Ce 3d transitions. However, in this work the Al source was mainly used because of the overlap between the Ce Auger electrons and the Mn 2p transitions, observed with the Mg source, severely affecting the Mn spectra due to the low signal-to-noise ratio. As expected, it is possible to visualize the elements Ce, O, Mn and C, confirming the high purity of the samples.
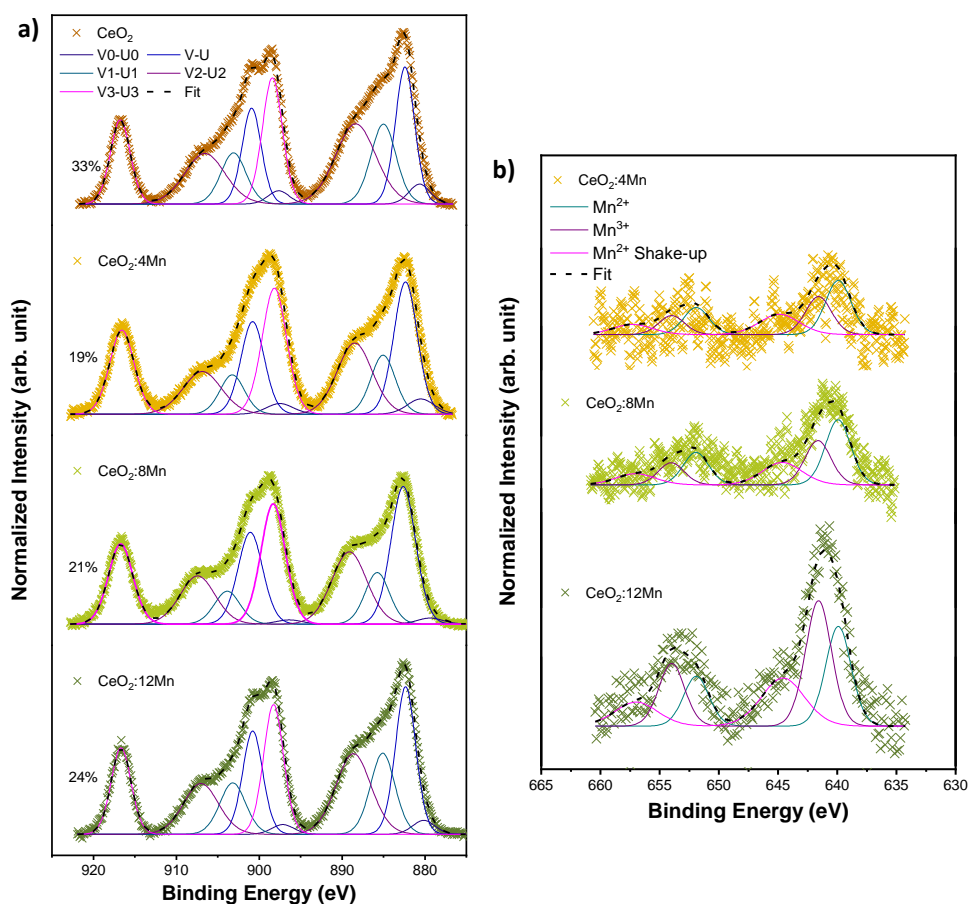


**Figure 4** – (A) XPS survey with the $Ce^{3+}$ percentage and (B) the Mn 2p spectra of the Mn-doped $CeO_2$ samples.

According to the literature [65], the interpretation of the Ce 3d spectra can be made by assuming a model of five spin-orbit coupled doublets (Ce $3d_{5/2}$ and Ce $3d_{3/2}$): two for $Ce^{3+}$ oxidation states and three for $Ce^{4+}$ oxidation states (labeled in Figure 4A as V0-U0 and V1-U1, and V-U, V2-U2 and V3-U3, respectively). These complex features have their origin in the hybridization of Ce 4f with O 2p binding orbitals and the partial occupation of the orbitals in the 4f valence state, giving rise to a well-known "shake-up" process, with some reports depicting 6 to 10 characteristic peaks [66, 67]. In this way, our results confirm the presence of $Ce^{4+}$ and $Ce^{3+}$ oxidation states in all studied samples. The amount of $Ce^{4+}$ and $Ce^{3+}$, corresponding to the $[CeO_8]$ and $[CeO_8.V_o^i]$ clusters, respectively, can be correlated with the U3 peak derived from the transition between $4f^0$ initial and final states. Since $Ce^{3+}$ does not have this configuration, U3 becomes the fingerprint of the $Ce^{4+}$ species. Assuming the occurrence of a uniform mixture of both oxidation states, the U3 peak intensity relative to the sum of all contributions to the Ce 3d region can be used to quantify the amount of $Ce^{4+}$ ($Ce^{3+}$) present on the sample surface. Even though the XPS technique can overestimate the $Ce^{3+}/Ce^{4+}$ ratio due to a possible photo-reduction process [68], a first decrease in the $Ce^{3+}$ proportion from 33 to 19% can be seen when comparing the pure and the 4wt%-doped samples, respectively, followed by a slight increase from 21 to 24% resulting from the already known metal promotion effect on ceria reduction [69–71]. The observed trend in the $Ce^{3+}$ proportion was also corroborated by the XPS analysis of the O 1s region shown in **Figure S1B** [72, 73]. In this sense, Aragón et al. [74] studied the influence of Fe-doping on $CeO_2$ and observed, through XPS data, a coexistence of $Ce^{3+}$ and $Ce^{4+}$ ions as well as a decreasing tendency of the relative fraction of $Ce^{3+}$ ions while increasing the iron content.

**Figure 4B** displays the Mn 2p spectra of the Mn-doped $CeO_2$ samples. As already mentioned, the low metal superficial concentration of these samples leads to a poor signal-to-noise ratio. Nevertheless, the obtained data evidence the typical spin-orbit coupled structure expected for Mn $2p_{3/2}$ and Mn $2p_{1/2}$. Going deeper into this analysis, it is known that Mn can have several oxidation states from 0 to 8+, with some of them (i.e., $Mn^{2+}$, $Mn^{3+}$, and $Mn^{4+}$ species) containing unpaired d electrons that originate multiple splitting XPS structures that (partially or totally) overlap, making it difficult to assign the correct species when these three oxidation states are present altogether [75]. In this context and based on our EPR results, we propose a simplified three spin-orbit coupled doublet model for the deconvolution of the Mn 2p region, which was tested with sample $CeO_2$:12Mn and then propagated to the data obtained for the samples with lower Mn content. This model indicates that our XPS data are consistent with the presence of both $Mn^{2+}$, with the main peak and its characteristic "shake-up" structure being located at 640.0 and 644.6 eV, respectively, and $Mn^{3+}$, with the main peak appearing at 641.6 eV. However, the existence of $Mn^{4+}$ cannot be ruled out due to the full signal overlap that occurs between them and $Mn^{3+}$ species, corroborating the EPR data.

The atomic concentrations obtained from the deconvoluted spectra of the samples are summarized in **Table 1**. As observed, the pure system has 33% of its cerium species in the $Ce^{3+}$ configuration, which would lead to a complementary fraction of 67% of $Ce^{4+}$. When the system is modified with 4 wt% Mn, there is an abrupt decrease in the amount of $Ce^{3+}$ species to 19%, suggesting that 14% of the $Ce^{3+}$ species are donating one electron to the $Mn^{2+}$ ions entering the lattice, thus becoming non-paramagnetic $Ce^{4+}$ species, which at first sight would indicate a reduction in the intensity of the EPR signal. On the other hand, 58% of the manganese species still remain in the $Mn^{2+}$ configuration with five unpaired electrons, justifying the paramagnetic feature of these samples. By increasing the Mn content from 4 to 8 wt%, there is an increase in the amount of $Ce^{3+}$ from 19 to 21%, while the amount of $Mn^{2+}$ is kept virtually constant, increasing only 1%, along with a decrease in the $Mn^{3+}$ configuration from 42 to 41%. By modifying the content of Mn to 12 wt%, another increase in the amount of $Ce^{3+}$ from 21 to 24% can be observed, together with a sudden decrease in the amount of $Mn^{2+}$ from 59 to 44% and an increase in the $Mn^{3+}$ configuration from 41 to 56%, which is EPR-silent. In this case, we can consider that the $Mn^{2+}$ ions are donating one electron, becoming $Mn^{3+}$, but not to the $Ce^{3+}$ species, since they also increase in concentration. Thus, these charges are likely transferred to neighboring defective neutral oxygen clusters, which then become singly ionized, enhancing the paramagnetic behavior of the sample.

Table 1 - Surface percentage of atomic concentrations from the deconvoluted spectra of **Figure 4**.

| Sample | %Ce$^{3+}$ | %Ce$^{3+}$ | %Mn$^{2+}$ | %Mn$^{3+}$ |
|---|---|---|---|---|
| CeO$_2$ | 33 | 67 | - | - |
| CeO$_2$:4Mn | 19 | 81 | 58 | 42 |
| CeO$_2$:8Mn | 21 | 79 | 59 | 41 |
| CeO$_2$:12Mn | 24 | 76 | 44 | 56 |

To get more insight into the surface species dynamics, sample CeO$_2$:12Mn was analyzed after an *in situ* reduction treatment in H$_2$ flow (70 ml/min) for 1 h at 400 °C and after an *ex situ* CO atmosphere treatment. It is known that the application of treatments with H$_{2(g)}$ and CO$_{(g)}$ to ceria can create V$_O^i$ [76, 77]. In this way, our aim was to understand the experimental mechanism responsible for the electronic exchanges between $Ce^{3+}$ and $Mn^{2+}$ species that generate the dipoles and quadrupoles seen in **Figure 3**, which can donate and receive electrons. **Figure 5** shows the Ce 3d and Mn 2p spectra obtained for the treated samples. The untreated sample (CeO$_2$:12Mn) was also included as a reference. As observed, after reduction the $Ce^{3+}$ species increase from 24 to 35% due to the Mn promotion effect associated with V$_O^i$ mobility [78, 79]. Likewise, the $Ce^{3+}$ concentration also increases up to 30% after CO atmosphere treatment, in line with what was previously reported by

Rocha et al. for La-doped $CeO_2$ [66]. Accordingly, the $Mn^{2+}$ and $Mn^{3+}$ are kept virtually constant under treatment in both atmospheres at 43 and 57%, respectively, compared to 44 and 56% for $CeO_2$:12Mn.
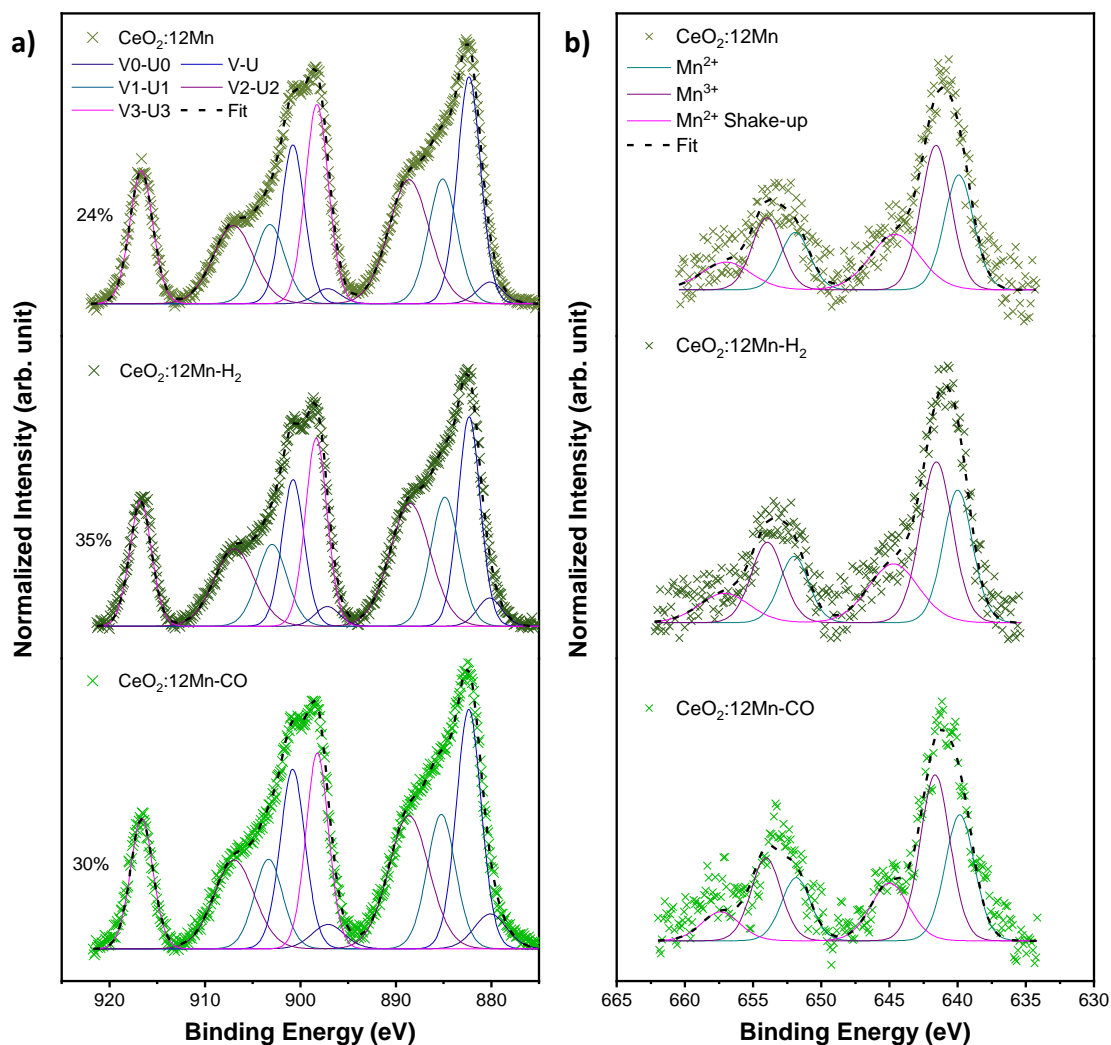


**Figure 5** – (A) Ce 3d and (B) Mn 2p XPS spectra for the treated samples.

## 4) Conclusions

Mn-doped ceria nanostructures were obtained using the MAH route after calcination at 500 °C, showing particle sizes below 40 nm. Raman and EPR analyses indicated the absence of Mn-O bonds as well as the presence of Mn-based defective clusters during interaction with CO. An increase in the number of paramagnetic species with increasing the Mn content was observed. This was assigned to the presence of $Mn^{2+}$ species resulting from the reduction of $Mn^{3+}$ after interaction with CO. The association of $Ce^{3+}$ and $Mn^{2+}$ species with $V_O$· seemed to be the most probable charge compensating defect, since their number reduced along with particle size with increasing the Mn concentration. The

XPS data confirmed the oxidation of some $Mn^{2+}$ to $Mn^{3+}$ and likely to $Mn^{4+}$, in addition to an increase in the number of $Ce^{3+}$ species.

**5) Author information**

**Corresponding Author**

**Marcelo Assis** – Department of Analytical and Physical Chemistry, University Jaume I (UJI), Av. Vicent Sos Baynat s/n, Castelló, 12071, Spain. *marcelostassis@gmail.com

**Miguel A. Ponce** – Advanced Materials Interdisciplinary Laboratory (LIMAV), Federal University of Itajubá (UNIFEI), Itabira, 37500-903, Brazil; Physics and Engineering Research Center, National University of the Center of the Province of Buenos Aires (UNCPBA-CICPBA-CONICET), Tandil, B7000GHG, Argentina; Institute of Materials Science and Technology (INTEMA), University of Mar del Plata (UNMdP), CONICET, Mar del Plata, B7606FWV, Argentina. *mponce.sensors@gmail.com

**Authors**

**Daniel C. Amaral** – Advanced Materials Interdisciplinary Laboratory (LIMAV), Federal University of Itajubá (UNIFEI), Itabira, 37500-903, Brazil.

**Leandro S. R. Rocha** – Center for Research and Development of Functional Materials (CDMF), Federal University of São Carlos (UFSCar), São Carlos, 13565-90, Brazil.

**Luis I. Granone** – Department of Chemistry and Biochemistry, FCEyN/IFIMAR, CONICET, National University of Mar del Plata, Mar del Plata, B7606FWV, Argentina.

**Mario M. Lage** – Advanced Materials Interdisciplinary Laboratory (LIMAV), Federal University of Itajubá (UNIFEI), Itabira, 37500-903, Brazil.

**Maria S. Churio** – Department of Chemistry and Biochemistry, FCEyN/IFIMAR, CONICET, National University of Mar del Plata, Mar del Plata, B7606FWV, Argentina.

**Miguel D. Sanchez** – Instituto de Física del Sur (IFISUR), Departamento de Física, Universidad Nacional del Sur (UNS), CONICET, Bahía Blanca, B8000CPB, Argentina

**Elson Longo**–Center for Research and Development of Functional Materials (CDMF), Federal University of São Carlos (UFSCar), São Carlos, 13565-90, Brazil.

**Hugo M. S. Nascimento**–Advanced Materials Interdisciplinary Laboratory (LIMAV), Federal University of Itajubá (UNIFEI), Itabira, 37500-903, Brazil.

**Francisco Moura** – Advanced Materials Interdisciplinary Laboratory (LIMAV), Federal University of Itajubá (UNIFEI), Itabira, 37500-903, Brazil.

The manuscript was written through the contributions of all authors. All authors have given approval to the final version of the manuscript.

**Notes**

**Supporting Information**

XPS survey and O1s high-resolution XPS spectra of the samples.

**References**

1. Acharya S, Bandyopadhyay A, Modak S, Mukherjee S, Das D, Chakrabarti PK (2009) XRD, HRTEM, magnetic and Mössbauer studies on chemically prepared Fe3+-doped nanoparticles of cerium oxide. Journal of Magnetism and Magnetic Materials 321:2701–2706. https://doi.org/10.1016/j.jmmm.2009.03.071

2. Lipp MJ, Jeffries JR, Cynn H, Park Klepeis J-H, Evans WJ, Mortensen DR, Seidler GT, Xiao Y, Chow P (2016) Comparison of the high-pressure behavior of the cerium oxides Ce2O3 and CeO2. Phys Rev B 93:064106. https://doi.org/10.1103/PhysRevB.93.064106

3. Proetto C, López A (1982) Magnetic exchange interactions in cerium compounds. Phys Rev B 25:7037–7039. https://doi.org/10.1103/PhysRevB.25.7037

4. Engelhardt LM, Figgis BN (1969) Magnetic susceptibility of cerium oxides. J Chem Soc A 2933–2937. https://doi.org/10.1039/J19690002933

5. Moreno H, Domingues GL, Assis M, Ortega PP, Mastelaro VR, Ramirez MA, Simões AZ (2023) The Relationship between Photoluminescence Emissions and Photocatalytic Activity of CeO2 Nanocrystals. Inorg Chem 62:4291–4303. https://doi.org/10.1021/acs.inorgchem.2c04411

6. Simonenko TL, Simonenko NP, Mokrushin AS, Simonenko EP, Glumov OV, Mel'nikova NA, Murin IV, Kalinina MV, Shilova OA, Sevastyanov VG, Kuznetsov NT (2020) Microstructural, electrophysical and gas-sensing properties of $CeO_2$–$Y_2O_3$ thin films obtained by the sol-gel process. Ceramics International 46:121–131. https://doi.org/10.1016/j.ceramint.2019.08.241

7. Tian D, Li K, Wei Y, Zhu X, Zeng C, Cheng X, Zheng Y, Wang H (2018) DFT insights into oxygen vacancy formation and $CH_4$ activation over $CeO_2$ surfaces modified by transition metals (Fe, Co and Ni). Phys Chem Chem Phys 20:11912–11929. https://doi.org/10.1039/C7CP08376A

8. Brant AT, Giles NC, Yang S(杨山), Sarker MAR, Watauchi S, Nagao M, Tanaka I, Tryk DA, Manivannan A, Halliburton LE (2013) Ground state of the singly ionized oxygen vacancy in rutile $TiO_2$. Journal of Applied Physics 114:113702. https://doi.org/10.1063/1.4819805

9. Montini T, Melchionna M, Monai M, Fornasiero P (2016) Fundamentals and Catalytic Applications of $CeO_2$-Based Materials. Chem Rev 116:5987–6041. https://doi.org/10.1021/acs.chemrev.5b00603

10. Lucian Pîslaru-Dănescu, Gabriela Telipan, Ioana Ion, Virgil Marinescu (2018) Prototyping a Gas Sensors Using $CeO_2$ as a Matrix or Dopant in Oxide Semiconductor Systems. In: Sher Bahadar Khan, Kalsoom Akhtar (eds) Cerium Oxide. IntechOpen, Rijeka, p Ch. 5

11. Qi J, Zhao K, Li G, Gao Y, Zhao H, Yu R, Tang Z (2014) Multi-shelled $CeO_2$ hollow microspheres as superior photocatalysts for water oxidation. Nanoscale 6:4072–4077. https://doi.org/10.1039/C3NR06822F

12. Aboud AA, Al-Kelesh H, Rouby WMAE, Farghali AA, Hamdedein A, Khedr MH (2018) $CO_2$ responses based on pure and doped $CeO_2$ nano-pellets. Journal of Materials Research and Technology 7:14–20. https://doi.org/10.1016/j.jmrt.2017.03.003

13. Simonenko TL, Kalinina MV, Simonenko NP, Simonenko EP, Glumov OV, Mel'nikova NA, Murin IV, Shichalin OO, Papynov EK, Shilova OA, Sevastyanov VG, Kuznetsov NT (2019) Synthesis of $BaCe_{0.9-x}Zr_xY_{0.1}O_{3-\delta}$ nanopowders and the study of proton conductors fabricated on their basis by low-temperature spark plasma sintering. International Journal of Hydrogen Energy 44:20345–20354. https://doi.org/10.1016/j.ijhydene.2019.05.231

14. Gopal CB, van de Walle A (2012) Ab initio thermodynamics of intrinsic oxygen vacancies in ceria. Phys Rev B 86:134117. https://doi.org/10.1103/PhysRevB.86.134117

15. Huang B, Gillen R, Robertson J (2014) Study of $CeO_2$ and Its Native Defects by Density Functional Theory with Repulsive Potential. J Phys Chem C 118:24248–24256. https://doi.org/10.1021/jp506625h

16. Ali A, Raza R, Khalil RMA, Ahmad MA, Rafique A, Ullah MK, Rehman A ur, Mushtaq MN, Belova LM (2018) A potential electrolyte ($Ce_{1-x}Ca_xO_{2-\delta}$) for fuel cells:Theoretical and experimental study. Ceramics International 44:12676–12683. https://doi.org/10.1016/j.ceramint.2018.04.068

17. Simonenko TL, Kalinina MV, Simonenko NP, Simonenko EP, Glumov OV, Mel'nikova NA, Murin IV, Shichalin OO, Papynov EK, Shilova OA (2018) Spark plasma sintering of nanopowders in the $CeO_2$-$Y_2O_3$ system as a promising approach to the creation of nanocrystalline intermediate-temperature solid electrolytes. Ceramics International 44:19879–19884. https://doi.org/10.1016/j.ceramint.2018.07.249

18. Fernandes Vaz IC, Tolentino Cabral AC, Silva Procópio AM, Moura Filho F (2022) Films based on cerium oxide sensitive to carbon monoxide. Materials Letters 308:131174. https://doi.org/10.1016/j.matlet.2021.131174

19. Pradhan N (2019) Mn-Doped Semiconductor Nanocrystals: 25 Years and Beyond. J Phys Chem Lett 10:2574–2577. https://doi.org/10.1021/acs.jpclett.9b01107

20. Dismukes GC, Sheats JE, Smegal JA (1987) Mn2+/Mn3+ and Mn3+/Mn4+ mixed valence binuclear manganese complexes of biological interest. J Am Chem Soc 109:7202–7203. https://doi.org/10.1021/ja00257a057

21. Xiao M, Zhang X, Yang Y, Cui X, Chen T, Wang Y (2022) M (M = Mn, Co, Cu)-CeO2 catalysts to enhance their CO catalytic oxidation at a low temperature: Synergistic effects of the interaction between Ce3+-Mx+-Ce4+ and the oxygen vacancy defects. Fuel 323:124379. https://doi.org/10.1016/j.fuel.2022.124379

22. El-Achari T, Goumrhar F, Drissi LB, Laamara RA (2021) Structural, electronic and magnetic properties of Mn doped CeO2: An ab-initio study. Physica B: Condensed Matter 601:412443. https://doi.org/10.1016/j.physb.2020.412443

23. Yu X, Wu X, Chen Z, Huang Z, Jing G (2019) Oxygen vacancy defect engineering in Mn-doped CeO2 nanostructures for nitrogen oxides emission abatement. Molecular Catalysis 476:110512. https://doi.org/10.1016/j.mcat.2019.110512

24. Qi G, Yang RT (2004) Characterization and FTIR Studies of MnOx−CeO2 Catalyst for Low-Temperature Selective Catalytic Reduction of NO with NH3. J Phys Chem B 108:15738–15747. https://doi.org/10.1021/jp048431h

25. Zimou J, Nouneh K, Hsissou R, El-Habib A, Gana LE, Talbi A, Beraich M, Lotfi N, Addou M (2021) Structural, morphological, optical, and electrochemical properties of Co-doped CeO2 thin films. Materials Science in Semiconductor Processing 135:106049. https://doi.org/10.1016/j.mssp.2021.106049

26. Murugan R, Vijayaprasath G, Mahalingam T, Ravi G (2016) Defect induced magnetic transition in Co doped CeO2 sputtered thin films. Ceramics International 42:11724–11731. https://doi.org/10.1016/j.ceramint.2016.04.091

27. Schilling C, Hofmann A, Hess C, Ganduglia-Pirovano MV (2017) Raman Spectra of Polycrystalline CeO2: A Density Functional Theory Study. J Phys Chem C 121:20834–20849. https://doi.org/10.1021/acs.jpcc.7b06643

28. Tuller HL, Nowick AS (1977) Small polaron electron transport in reduced CeO2 single crystals. Journal of Physics and Chemistry of Solids 38:859–867. https://doi.org/10.1016/0022-3697(77)90124-X

29. Yamazoe N, Fuchigami J, Kishikawa M, Seiyama T (1979) Interactions of tin oxide surface with O2, H2O AND H2. Surface Science 86:335–344. https://doi.org/10.1016/0039-6028(79)90411-4

30. Batzill M, Diebold U (2005) The surface and materials science of tin oxide. Progress in Surface Science 79:47–154. https://doi.org/10.1016/j.progsurf.2005.09.002

31. Phokha S, Pinitsoontorn S, Chirawatkul P, Poo-arporn Y, Maensiri S (2012) Synthesis, characterization, and magnetic properties of monodisperse CeO2 nanospheres prepared by PVP-

assisted hydrothermal method. Nanoscale Research Letters 7:425. https://doi.org/10.1186/1556-276X-7-425

32. Kosacki I, Suzuki T, Anderson HU, Colomban P (2002) Raman scattering and lattice defects in nanocrystalline CeO2 thin films. Solid State Ionics 149:99–105. https://doi.org/10.1016/S0167-2738(02)00104-2

33. Weber WH, Hass KC, McBride JR (1993) Raman study of CeO2: Second-order scattering, lattice dynamics, and particle-size effects. Phys Rev B 48:178–185. https://doi.org/10.1103/PhysRevB.48.178

34. Korepanov VI, Hamaguchi H (2017) Quantum-chemical perspective of nanoscale Raman spectroscopy with the three-dimensional phonon confinement model. Journal of Raman Spectroscopy 48:842–846. https://doi.org/10.1002/jrs.5132

35. Zhang X, Qiao X-F, Shi W, Wu J-B, Jiang D-S, Tan P-H (2015) Phonon and Raman scattering of two-dimensional transition metal dichalcogenides from monolayer, multilayer to bulk material. Chem Soc Rev 44:2757–2785. https://doi.org/10.1039/C4CS00282B

36. Yang S, Zhang Y (2022) Spectroscopic ellipsometry study of Mn doped CeO2 thin films prepared by radio-frequency magnetron sputtering. Thin Solid Films 760:139516. https://doi.org/10.1016/j.tsf.2022.139516

37. Conceição EJF, Aragón FFH, Urian YA, Castro TJ, Coaquira JAH, Morais PC, da Silva SW (2023) Effects of Gd doping on the structural, optical and magnetic properties of Ce1−xGdxO2−δ nanoparticles and the impact of the oxygen vacancy. Journal of Alloys and Compounds 960:170628. https://doi.org/10.1016/j.jallcom.2023.170628

38. Endres SC, Ciacchi LC, Mädler L (2021) A review of contact force models between nanoparticles in agglomerates, aggregates, and films. Journal of Aerosol Science 153:105719. https://doi.org/10.1016/j.jaerosci.2020.105719

39. Zhou Y, Ren S, Wang M, Yang J, Chen Z, Chen L (2021) Mn and Fe oxides co-effect on nanopolyhedron CeO2 catalyst for NH3-SCR of NO. Journal of the Energy Institute 99:97–104. https://doi.org/10.1016/j.joei.2021.08.003

40. Chen P-L, Chen I-W (1996) Grain Growth in CeO2: Dopant Effects, Defect Mechanism, and Solute Drag. Journal of the American Ceramic Society 79:1793–1800. https://doi.org/10.1111/j.1151-2916.1996.tb07997.x

41. Mani Rahulan K, Angeline Little Flower N, Annie Sujatha R, Mohana Priya P, Gopalakrishnan C (2018) Third order nonlinear optical properties of Mn doped CeO2 nanostructures. Optics & Laser Technology 101:358–362. https://doi.org/10.1016/j.optlastec.2017.11.041

42. Lee K-M, Brito M, DeCoster J, Linskens K, Mehdi K, Lee W-I, Kim E, Kim H, Kwon G, Nam C-Y, Kim T (2022) Influence of oxidizing and reducing pretreatment on the catalytic performance of CeO2 for CO oxidation. Molecular Catalysis 528:112465. https://doi.org/10.1016/j.mcat.2022.112465

43. Prohaska J, Trömel M, Rager H (1993) EPR study of Fe3+ and Mn2+ in CeO2 and ThO2. Applied Magnetic Resonance 5:387–398. https://doi.org/10.1007/BF03162535

44. García Pintos D, Juan A, Irigoyen B (2013) Mn-Doped CeO2: DFT+U Study of a Catalyst for Oxidation Reactions. J Phys Chem C 117:18063–18073. https://doi.org/10.1021/jp403911b

45. Mansoor H, Harrigan WL, Lehuta KA, Kittilstved KR (2019) Reversible Control of the Mn Oxidation State in SrTiO3 Bulk Powders. Frontiers in Chemistry 7:

46. Popov AL, Popova NR, Selezneva II, Akkizov AY, Ivanov VK (2016) Cerium oxide nanoparticles stimulate proliferation of primary mouse embryonic fibroblasts in vitro. Materials Science and Engineering: C 68:406–413. https://doi.org/10.1016/j.msec.2016.05.103

47. Dashdorj J, Zvanut ME, Stanley LJ (2010) Iron-related defect levels in SrTiO3 measured by photoelectron paramagnetic resonance spectroscopy. Journal of Applied Physics 107:083513. https://doi.org/10.1063/1.3372760

48. Kakazey M, Ivanova N, Boldurev Y, Ivanov S, Sokolsky G, Gonzalez-Rodriguez JG, Vlasova M (2003) Electron paramagnetic resonance in MnO2 powders and comparative estimation of electric characteristics of power sources based on them in the MnO2–Zn system. Journal of Power Sources 114:170–175. https://doi.org/10.1016/S0378-7753(02)00595-5

49. Hemantha Kumar GN, Lakshmana Rao J, Gopal NO, Narasimhulu KV, Chakradhar RPS, Varada Rajulu A (2004) Spectroscopic investigations of Mn2+ ions doped polyvinylalcohol films. Polymer 45:5407–5415. https://doi.org/10.1016/j.polymer.2004.05.068

50. Rakhmatullin RM, Semashko VV, Korableva SL, Kiiamov AG, Rodionov AA, Tschaggelar R, van Bokhoven JA, Paun C (2018) EPR study of ceria nanoparticles containing different concentration of Ce3+ ions. Materials Chemistry and Physics 219:251–257. https://doi.org/10.1016/j.matchemphys.2018.08.028

51. Burbano M, Marrocchelli D, Yildiz B, Tuller HL, Norberg ST, Hull S, Madden PA, Watson GW (2011) A dipole polarizable potential for reduced and doped CeO2 obtained from first principles. Journal of Physics: Condensed Matter 23:255402. https://doi.org/10.1088/0953-8984/23/25/255402

52. R A Gordon, M W Haverkort, Subhra Sen Gupta, G A Sawatzky (2009) Orientation-dependent x-ray Raman scattering from cubic crystals: Natural linear dichroism in MnO and CeO2. Journal of Physics: Conference Series 190:012047. https://doi.org/10.1088/1742-6596/190/1/012047

53. Fuda K, Kishio K, Yamauchi S, Fueki K, Onoda Y (1984) 17 O NMR study of Y2O3-doped CeO2. Journal of Physics and Chemistry of Solids 45:1253–1257. https://doi.org/10.1016/0022-3697(84)90024-6

54. Vaz ICF, Macchi CE, Somoza A, Rocha LSR, Longo E, Cabral L, da Silva EZ, Simões AZ, Zonta G, Malagù C, Desimone PM, Ponce MA, Moura F (2022) Electrical transport mechanisms of Neodymium-doped rare-earth semiconductors. Journal of Materials Science: Materials in Electronics 33:11632–11649. https://doi.org/10.1007/s10854-022-08098-9

55. Esch F, Fabris S, Zhou L, Montini T, Africh C, Fornasiero P, Comelli G, Rosei R (2005) Electron localization determines defect formation on ceria substrates. Science 309:752–755. https://doi.org/10.1126/science.1111568

56. Wang L, Yu Y, He H, Zhang Y, Qin X, Wang B (2017) Oxygen vacancy clusters essential for the catalytic activity of CeO2 nanocubes for o-xylene oxidation. Scientific Reports 7:12845. https://doi.org/10.1038/s41598-017-13178-6

57. Thajudheen T, Dixon AG, Gardonio S, Arčon I, Valant M (2020) Oxygen Vacancy-Related Cathodoluminescence Quenching and Polarons in CeO2. J Phys Chem C 124:19929–19936. https://doi.org/10.1021/acs.jpcc.0c04631

58. Su Z, Yang W, Wang C, Xiong S, Cao X, Peng Y, Si W, Weng Y, Xue M, Li J (2020) Roles of Oxygen Vacancies in the Bulk and Surface of CeO2 for Toluene Catalytic Combustion. Environ Sci Technol 54:12684–12692. https://doi.org/10.1021/acs.est.0c03981

59. Das T, Nicholas JD, Sheldon BW, Qi Y (2018) Anisotropic chemical strain in cubic ceria due to oxygen-vacancy-induced elastic dipoles. Phys Chem Chem Phys 20:15293–15299. https://doi.org/10.1039/C8CP01219A

60. Velu S, Shah N, Jyothi TM, Sivasanker S (1999) Effect of manganese substitution on the physicochemical properties and catalytic toluene oxidation activities of Mg–Al layered double hydroxides. Microporous and Mesoporous Materials 33:61–75. https://doi.org/10.1016/S1387-1811(99)00123-7

61. Saab E, Aouad S, Abi-Aad E, Zhilinskaya E, Aboukaïs A (2007) Carbon black oxidation in the presence of Al2O3, CeO2, and Mn oxide catalysts: An EPR study. Catalysis Today 119:286–290. https://doi.org/10.1016/j.cattod.2006.08.031

62. Al-Agel FA, Al-Arfaj E, Al-Ghamdi AA, Losovyj Y, Bronstein LM, Mahmoud WE (2014) A novel recipe to improve the magnetic properties of Mn doped CeO2 as a room temperature ferromagnetic diluted metal oxide. Journal of Magnetism and Magnetic Materials 360:73–79. https://doi.org/10.1016/j.jmmm.2014.02.013

63. Hong W-J, Iwamoto S, Hosokawa S, Wada K, Kanai H, Inoue M (2011) Effect of Mn content on physical properties of CeOx–MnOy support and BaO–CeOx–MnOy catalysts for direct NO decomposition. Journal of Catalysis 277:208–216. https://doi.org/10.1016/j.jcat.2010.11.007

64. Zhang J, Wong H, Yu D, Kakushima K, Iwai H (2014) X-ray photoelectron spectroscopy study of high-k CeO2/La2O3 stacked dielectrics. AIP Advances 4:117117. https://doi.org/10.1063/1.4902017

65. Rocha LSR, Aparecido Ciola Amoresi R, Duarte TM, Marana NL, Sambrano JR, Aldao CM, Simões AZ, Ponce MA, Longo E (2020) Experimental and theoretical interpretation of the order/disorder clusters in CeO2:La. Applied Surface Science 510:145216. https://doi.org/10.1016/j.apsusc.2019.145216

66. Bêche E, Charvin P, Perarnau D, Abanades S, Flamant G (2008) Ce 3d XPS investigation of cerium oxides and mixed cerium oxide (CexTiyOz). Surface and Interface Analysis 40:264–267. https://doi.org/10.1002/sia.2686

67. Cardenas L, Molinet-Chinaglia C, Loridant S (2022) Unraveling Ce3+ detection at the surface of ceria nanopowders by UPS analysis. Phys Chem Chem Phys 24:22815–22822. https://doi.org/10.1039/D2CP02736D

68. Cong Q, Chen L, Wang X, Ma H, Zhao J, Li S, Hou Y, Li W (2020) Promotional effect of nitrogen-doping on a ceria unary oxide catalyst with rich oxygen vacancies for selective catalytic reduction of NO with NH3. Chemical Engineering Journal 379:122302. https://doi.org/10.1016/j.cej.2019.122302

69. Clark AH, Marchbank HR, Thompsett D, Fisher JM, Longo A, Beyer KA, Hyde TI, Sankar G (2022) On the effect of metal loading on the reducibility and redox chemistry of ceria supported Pd catalysts. Phys Chem Chem Phys 24:2387–2395. https://doi.org/10.1039/D1CP04654C

70. Acerbi N, Golunski S, Tsang SC, Daly H, Hardacre C, Smith R, Collier P (2012) Promotion of Ceria Catalysts by Precious Metals: Changes in Nature of the Interaction under Reducing and Oxidizing Conditions. J Phys Chem C 116:13569–13583. https://doi.org/10.1021/jp212233u

71. Della Mea GB, Matte LP, Thill AS, Lobato FO, Benvenutti EV, Arenas LT, Jürgensen A, Hergenröder R, Poletto F, Bernardi F (2017) Tuning the oxygen vacancy population of cerium oxide (CeO2−x, 0. Applied Surface Science 422:1102–1112. https://doi.org/10.1016/j.apsusc.2017.06.101

72. Soni S, Vats VS, Kumar S, Dalela B, Mishra M, Meena RS, Gupta G, Alvi PA, Dalela S (2018) Structural, optical and magnetic properties of Fe-doped $CeO_2$ samples probed using X-ray photoelectron spectroscopy. Journal of Materials Science: Materials in Electronics 29:10141–10153. https://doi.org/10.1007/s10854-018-9060-x

73. Aragón FFH, Aquino JCR, Ramos JE, Coaquira JAH, Gonzalez I, Macedo WAA, da Silva SW, Morais PC (2017) Fe-doping effects on the structural, vibrational, magnetic, and electronic properties of ceria nanoparticles. Journal of Applied Physics 122:204302. https://doi.org/10.1063/1.4999457

74. Biesinger MC, Payne BP, Grosvenor AP, Lau LWM, Gerson AR, Smart RStC (2011) Resolving surface chemical states in XPS analysis of first row transition metals, oxides and hydroxides: Cr, Mn, Fe, Co and Ni. Applied Surface Science 257:2717–2730. https://doi.org/10.1016/j.apsusc.2010.10.051

75. Li Z, Werner K, Chen L, Jia A, Qian K, Zhong J-Q, You R, Wu L, Zhang L, Pan H, Wu X-P, Gong X-Q, Shaikhutdinov S, Huang W, Freund H-J (2021) Interaction of Hydrogen with Ceria: Hydroxylation, Reduction, and Hydride Formation on the Surface and in the Bulk. Chemistry – A European Journal 27:5268–5276. https://doi.org/10.1002/chem.202005374

76. Jan A, Shin J, Ahn J, Yang S, Yoon KJ, Son J-W, Kim H, Lee J-H, Ji H-I (2019) Promotion of Pt/CeO2 catalyst by hydrogen treatment for low-temperature CO oxidation. RSC Adv 9:27002–27012. https://doi.org/10.1039/C9RA05965B

77. Yang M, Shen G, Wang Q, Deng K, Liu M, Chen Y, Gong Y, Wang Z (2021) Roles of Oxygen Vacancies of CeO2 and Mn-Doped CeO2 with the Same Morphology in Benzene Catalytic Oxidation. Molecules 26:. https://doi.org/10.3390/molecules26216363

78. Liu X, Zhou K, Wang L, Wang B, Li Y (2009) Oxygen Vacancy Clusters Promoting Reducibility and Activity of Ceria Nanorods. J Am Chem Soc 131:3140–3141. https://doi.org/10.1021/ja808433d